Angewandte Chemie International Edition

Angewandte International Edition Chemie

How to cite: *Angew. Chem. Int. Ed.* **2026**, e1626004
doi.org/10.1002/anie.1626004

RESEARCH ARTICLE OPEN ACCESS Hot Paper

Constructing p-d Orbital Hybridization via In Situ Generation of $Bi_{19}Br_3S_{27}/NiS_x$ for Highly Selective Photothermal CO_2 Reduction to C_2H_4

Guangmei Gan[1] | Zhixiong Yang[1] | Mengying Wang[1] | Yang Shi[2] | Yuan Li[1] | Gaoke Zhang[1] | Jie Wu[2]

[1]Hubei Key Laboratory of Mineral Resources Processing and Environment, Key Laboratory of Green Utilization of Critical Non-metallic Mineral Resources, Ministry of Education, State Key Laboratory of Silicate Materials for Architectures, Wuhan University of Technology, Wuhan, People's Republic of China | [2]Department of Chemistry, National University of Singapore, Singapore, Singapore

Correspondence: Gaoke Zhang (gkzhang@whut.edu.cn) | Jie Wu (chmjie@nus.edu.sg)

Received: 2 July 2026 | **Revised:** 23 August 2026 | **Accepted:** 9 September 2026

Keywords: CO_2 reduction | ethylene | high selectivity | orbital hybridization | photothermal catalysis

ABSTRACT

Photothermal catalytic CO_2 reduction to multi-carbon products is a promising approach for carbon utilization, yet the design of active sites that effectively promote multistep C—C coupling toward selective C_2H_4 formation remains a significant challenge. Hence, we employ an in situ interfacial engineering strategy to construct crystalline/amorphous $Bi_{19}Br_3S_{27}/NiS_x$ (BBSN) photothermal catalysts with strong p-d orbital hybridization. The optimized BBSN-8 achieves a C_2H_4 production rate of 41.38 μmol g^{-1} h^{-1} with a selectivity of 96.8% under full-spectrum irradiation, which exhibits a remarkable advantage in the field of C_2H_4 production. Experimental results and theoretical calculations demonstrate that Ni incorporation optimizes CO_2 adsorption from overly strong Bi—C single-site binding to balanced multi-sites adsorption, while newly formed p-d orbital hybridization establishes electronically cooperative Bi—S—Ni active sites stabilizing both carbon- and oxygen-centered species, synergistically facilitating *CO—CHO* coupling and boosting C_2H_4 formation. This work demonstrates that in situ interfacial orbital hybridization can regulate intermediate coupling and steer photothermal CO_2 reduction toward highly selective C_2H_4 formation.

1 | Introduction

The conversion of CO_2 into value-added multi-carbon products is widely regarded as a promising strategy for mitigating carbon emissions while addressing energy demands [1–3]. Among various products, ethylene (C_2H_4) holds particular importance due to its pivotal role in the chemical industry. Recently, photothermal catalysis has emerged as an effective approach to drive CO_2 conversion by integrating photo-induced carrier excitation with thermally accelerated surface reactions [4, 5]. However, the conversion of CO_2 to C_2H_4 over photothermal catalysts still suffers from limited selectivity, largely due to the involvement of complex multi-electron transfer processes and the requirement for dynamic C—C coupling steps [6–8]. To address this challenge, considerable efforts have been devoted to strategies such as band structure tuning and defect engineering, which have enhanced charge separation and adsorption properties [9, 10]. Despite these advances, achieving cooperative activation of multiple intermediates during C—C coupling remains difficult. In particular, the formation of C_2 products requires electronically differentiated active sites that could selectively interact with distinct moieties of reaction intermediates, which is difficult to establish within uniform coordination environment [11, 12].

Constructing electronic coupling between adjacent active centers is expected to enable coordinated interaction with reaction inter-

mediates. Orbital-level interactions provide an effective means to regulate such coupling by controlling how electrons are distributed and transferred during the reaction [13, 14]. Among various orbital interactions, p-d orbital hybridization between ligand p orbitals and transition-metal d orbitals is particularly attractive as it can simultaneously facilitate CO_2 activation and regulate the evolution of carbon-containing intermediates through synergistic σ-donation and π-backdonation processes [15, 16]. Such orbital coupling could induce molecular polarization and bending of CO_2, promoting electron injection into CO_2 antibonding orbitals and thus facilitating the formation of key intermediates [17, 18]. For example, lattice strain engineering in $BiFeO_3$ has been shown to optimize d/p-2π* orbital hybridization, thereby enhancing CO_2 activation and promoting *COOH intermediates formation [19]. More importantly, p-d orbital hybridization may further regulate the adsorption and evolution behaviors of carbon-containing intermediates, thereby influencing C—C coupling kinetics and the product selectivity. Notably, the p-d orbital hybridization in p-block metal-doped Cu catalysts was found to optimize *CO binding and facilitate *CO dimerization, thereby selectively directing CO_2 electroreduction toward C_{2+} products with a Faradaic efficiency of 81.5% [20]. Hence, the interaction between ligand p orbitals and transition metal d orbitals is expected to achieve highly selective generation of C_2 products. Nevertheless, achieving efficient p-d orbital hybridization generally requires strongly coupled interfacial electronic interactions to ensure continuous electron migration and effective orbital overlap [21, 22]. Therefore, employing suitable strategies to construct highly coupled interfaces is essential for maximizing the benefits of p-d orbital hybridization. In situ construction provides an effective approach for generating strongly coupled heterogeneous interfaces, which promotes the formation of an integrated bonding environment while suppressing electron isolation domains [23, 24]. However, the rational construction of effective p-d hybridization systems via in situ construction strategy is rarely reported.

Herein, we employ an in situ interfacial engineering strategy to construct $Bi_{19}Br_3S_{27}/NiS_x$ photothermal catalyst featuring p–d orbital hybridization for highly selective CO_2-to-C_2H_4 conversion. The in situ generated NiS_x induces a balanced multi-sites adsorption for CO_2 and constructs the interfacial orbital hybridization. Various results of experimental and characterization tests reveal that the newly formed p-d orbital hybridization promotes Bi—S—Ni cooperative interactions with CO_2 molecules, thereby facilitating selective C—C coupling toward C_2 pathway. As a result, the optimized BBSN-8 catalyst achieves a high C_2H_4 selectivity of 96.8% under full-spectrum light irradiation. This study not only provides new insights into the role of orbital hybridization in regulating complex reaction pathways but also offers a rational strategy for designing advanced catalysts for multi-carbon product generation from CO_2.

2 | Results and Discussion

2.1 | Structural and Morphological Properties

The crystalline/amorphous $Bi_{19}Br_3S_{27}/NiS_x$ (BBSN) was constructed through an in situ growth strategy, where amorphous NiS_x was in situ generated on crystalline $Bi_{19}Br_3S_{27}$ (BBS) nanoneedles under sulfur-rich hydrothermal conditions, forming an intimately coupled interface (Figure 1a). The obtained samples were denoted as BBSN-*x*, where *x* represents the molar ratio of Ni precursor to Bi during preparation. The actual Ni/Bi ratios determined by inductively coupled plasma optical emission spectroscopy (ICP-OES) are summarized in Table S1. The morphology and microstructure of BBSN were observed by transmission electron microscopy (TEM) characterizations. As displayed in Figure 1b, pristine BBS exhibits smooth-tipped nanoneedle structures. The interplanar spacing shown in Figure S1 is 0.294 nm and 0.532 nm, which are indexed to the (140) and (120) plane of $Bi_{19}Br_3S_{27}$, respectively. After Ni incorporation, an overlayer emerged on the BBS nanoneedles, exhibiting a thickness that scaled with the Ni content (Figure 1c and Figure S2). In particular, the high-resolution TEM (HRTEM) image of BBSN-8 (Ni/Bi = 8:100) in Figure 1d,e revealed a distinct crystalline-amorphous boundary, indicating the presence of an amorphous overlayer on the surface of BBS. To further identify the structure of crystalline/amorphous structure, the HRTEM characterization and the corresponding elemental mapping tests were conducted. As shown in Figure 1f, the Bi and Br elements are evenly dispersed throughout the whole nanoneedle tips, whereas the Ni element predominantly concentrated in the amorphous shell and S is uniformly distributed throughout the entire region. Furthermore, the energy-dispersive spectroscopy (EDS) line scanning profiles in Figure 1g showed that a gradual outward increase in Ni concentration. These results suggest that the outer amorphous layer consists of NiS_x, which is in situ formed on the BBS surface. The diffraction spots and diffraction rings in the corresponding selected-area fast fourier transform (FFT) patterns in Figure S3 further verifies the crystalline structure of BBS and the amorphous phase of NiS_x.

The phase structure of BBSN was analyzed by x-ray diffraction (XRD) and Raman characterizations. As illustrated in Figure 2a, all samples exhibit characteristic diffraction patterns corresponding to the hexagonal phase of $Bi_{19}Br_3S_{27}$ (JCPDS No. 70–0202), which verifies that BBS possesses high crystallinity. For the BBSN-*x* with different molar ratios of Ni/Bi, there were no new diffraction peaks emerged in the XRD patterns, but the peak intensity of BBS decreased slightly. This may be owing to the excess sulfur species released from thiourea during the synthesis process, which could readily react with Ni^{2+}, resulting in the preferential formation of NiS_x under sulfur-rich conditions. The Raman spectra were further used to detect the crystallinity of BBSN. Compared to BBS, the Raman spectrum of BBSN-8 with amorphous NiS_x exhibits a pronounced peak broadening at 264 cm^{-1} (Figure 2b), suggesting that the interaction of BBS with the introduction of Ni, which is in favor of surface reconstruction of BBS [25].

The surface chemical state evolution from BBS to BBSN-8 transformation was investigated through x-ray photoelectron spectroscopy (XPS) tests. The Bi 4f XPS spectra of BBS and BBSN-8 are shown in Figures 2c and S4. Two characteristic peaks emerge at the binding energies of 163.59 eV and 158.27 eV, corresponding to the Bi $4f_{7/2}$ and Bi $4f_{5/2}$, respectively [26]. After loading of NiS_x, the Bi 4f in BBSN-8 shifts 0.06 eV toward high binding energy compared to BBS, indicating that the electron cloud density around Bi decreased after deposition of NiS_x. This may be attributed to interfacial charge redistribution between

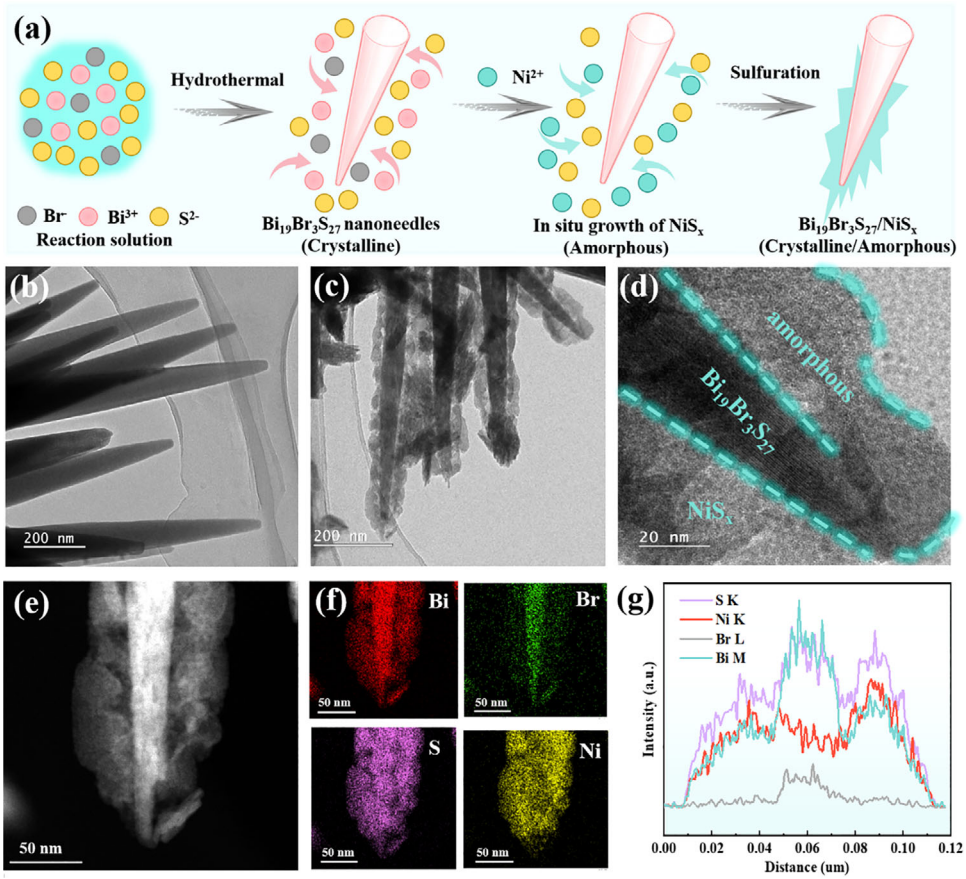

FIGURE 1 | (a) Schematic drawing of the synthesis route of $Bi_{19}Br_3S_{27}/NiS_x$. The TEM images of (b) BBS and (c) BBSN-8. (d) HRTEM, (e) HAADF-STEM, (f) corresponding elemental mappings, and (g) EDS line scanning profiles of BBSN-8.

BBS and NiS_x, wherein the sharing of S^{2-} drives the establishment of interfacial coupling that accelerates charge migration.

To probe the atomic coordination structure of BBSN-8, x-ray absorption near-edge structure spectra (XANES) measurements were carried out at the Ni K-edge. As shown in XANES spectra (Figure 2d), the absorption edge position of BBSN-8 closely overlaps with that of NiS, indicating that Ni predominantly exists in the +2 valence state. The Fourier transform extended x-ray absorption fine structure (FT-EXAFS) spectra in Figure 2e,f display an obvious peak at approximately 2.02 Å, corresponding to the first-shell Ni—S coordination, consistent with the Ni—S bond in NiS, confirming the formation of Ni—S bonds in BBSN-8 [25]. Notably, the weakened EXAFS intensity compared to NiS references implies a higher degree of disorder local structural around the Ni sites in BBSN-8. To gain deeper insight into the coordination environment, 3D wavelet transform-EXAFS (3D WT-EXAFS) analysis was further employed. As illustrated in Figure 2g–i, the 3D WT contour map of BBSN-8 exhibits a characteristic intensity feature located at ~2.1 Å along the Y radial distance axis, which matches well with the Ni—S scattering signal observed in NiS, while differing from that of NiO, thereby excluding significant Ni—O coordination. Quantitative EXAFS fitting results (Figures S5 and S6 and Table S2) confirm that Ni atoms are mainly coordinated with S atoms. Importantly, the coordination number of the Ni—S shell is significantly reduced (2.5) compared to crystalline NiS (CN = 6), indicating a highly unsaturated coordination environment [27]. Meanwhile, the negative ΔR values and relatively large Debye—Waller factors further confirm bond contraction and substantial structural disorder. Collectively, these results demonstrate that Ni species in BBSN-8 predominantly exist in a low-coordinated and structurally disordered Ni—S configuration.

2.2 | Photothermal Catalytic CO_2 Reduction

The photothermal catalytic performances of BBS and BBSN were evaluated under full-spectrum light irradiation (Figure S7). Product analysis by gas chromatography and nuclear magnetic resonance (^{1}H NMR spectroscopy) (Figure S8) tests reveal that C_2H_4 and CO are the primary carbon-containing products, while only trace amounts of H_2 are detected. Furthermore, a volcano-type trend of C_2H_4 yield and selectivity on BBS with different Ni loading is observed in Figures S9 and 3a. Under full-spectrum light illumination, the BBSN-8 catalyst achieves the highest activity (41.38 μmol g^{-1} h^{-1}) with a remarkable selectivity of 96.8%, representing an 8.8-fold increase compared to BBS (4.66 μmol g^{-1} h^{-1}, 81.5%). This significantly enhanced yield highlights the crucial role of NiS_x in promoting the rapid coupling of C_1 intermediates toward C_2H_4. To further assess the light-to-heat conversion ability, catalytic performance for BBSN-8 was evaluated under different irradiation intensities. As shown in Figure 3b, C_2H_4 yields increase substantially with increasing light

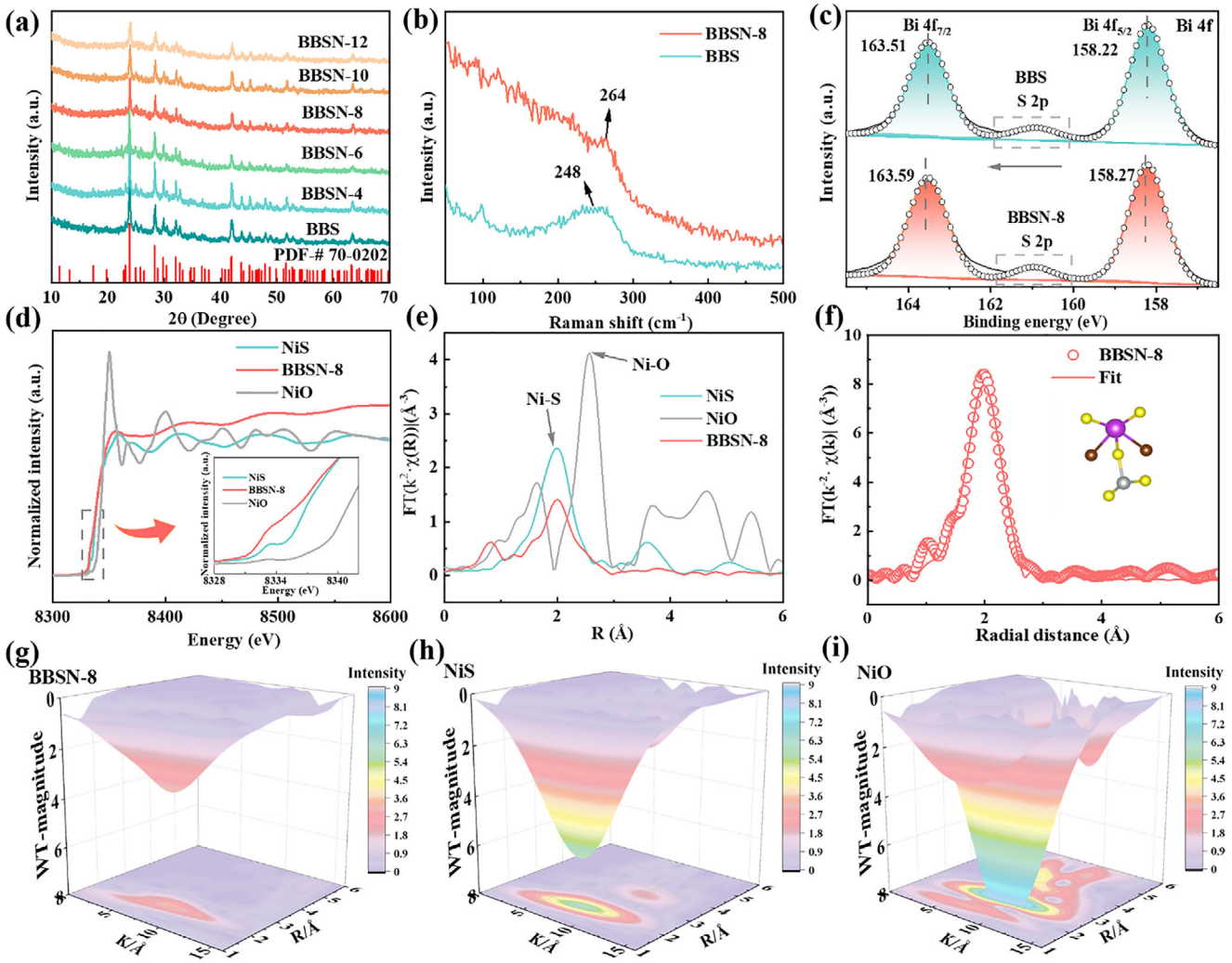

FIGURE 2 | (a) The XRD patterns of BBSN. (b) Raman spectra, (c) Bi 4f XPS spectra of BBS and BBSN-8. (d) XANES and (e) FT-EXAFS of Ni K-edge spectra for NiO, NiS, and BBSN-8. (f) EXAFS fitting results of Ni K-edge at k-space of BBSN-8. 3D WT-EXAFS at Ni K-edge for (g) BBSN-8, (h) NiS, and (i) NiO.

intensity from 0.2 to 0.68 W cm^{-2}. Notably, under concentrated solar irradiation (0.68 W cm^{-2}), BBSN-8 reaches an activity of 43.38 μmol g^{-1} h^{-1} with selectivity of 96.8%, which is 3.6 times higher than that of under non-concentrated illumination (11.92 μmol g^{-1} h^{-1}, 0.2 W cm^{-2}), underscoring the excellent photo-thermal conversion ability of BBSN-8 [28, 29]. Meanwhile, the results of surface temperature under different irradiation times showed that BBSN-8 reaches a notably higher steady-state temperature (240°C) than BBS (200°C) (Figure S10). This result further demonstrated that NiS_x incorporation significantly enhances light-to-heat conversion efficiency, which is closely associated with catalytic performance.

To further disentangle the contributions of thermal effects and photocatalytic effects over the BBSN-8, the CO_2 reduction experiments were conducted under distinct reaction environments. In dark at 240°C, BBSN exhibits a C_2H_4 yield of 23.39 μmol g^{-1} h^{-1} that accounts for 53.8% of C_2H_4 yield under full-spectrum light irradiation, indicating that thermal plays an important role in the C_2H_4 generation (Figure 3c). Besides, the apparent activation energy for C_2H_4 production decreases from 100.7 kJ mol^{-1} under thermal catalysis to 68.3 kJ mol^{-1} under full-spectrum light illumination (Figure 3d), indicating that the reaction kinetics are enhanced through the synergistic effect between photocatalytic and thermocatalytic processes. To further explore the underlying role of light, CO_2 reduction tests were subsequently carried out under different light sources. As shown in Figure 3e, the surface temperature of BBSN-8 under visible-near (Vis−NIR) light (190°C) is similar with that achieved under NIR light (180°C), while the C_2H_4 yield under Vis−NIR irradiation (28.1 μmol g^{-1} h^{-1}) is markedly higher than under NIR excitation (9.13 μmol g^{-1} h^{-1}), revealing that temperature rise induced by photothermal effect is not the sole driving force, and photoexcited charge carriers generated under light irradiation play a critical role in enabling C—C coupling toward C_2H_4. Combining these results, it could be concluded that the photothermal CO_2 conversion in BBSN is predominantly initiated by a synergistic process for photocatalytic and thermal catalytic reactions.

To identify the source of CO_2 reduction products over the BBSN-8 catalyst, a series of control experiments were performed. As illustrated in Figure 3f, no carbon-containing products were

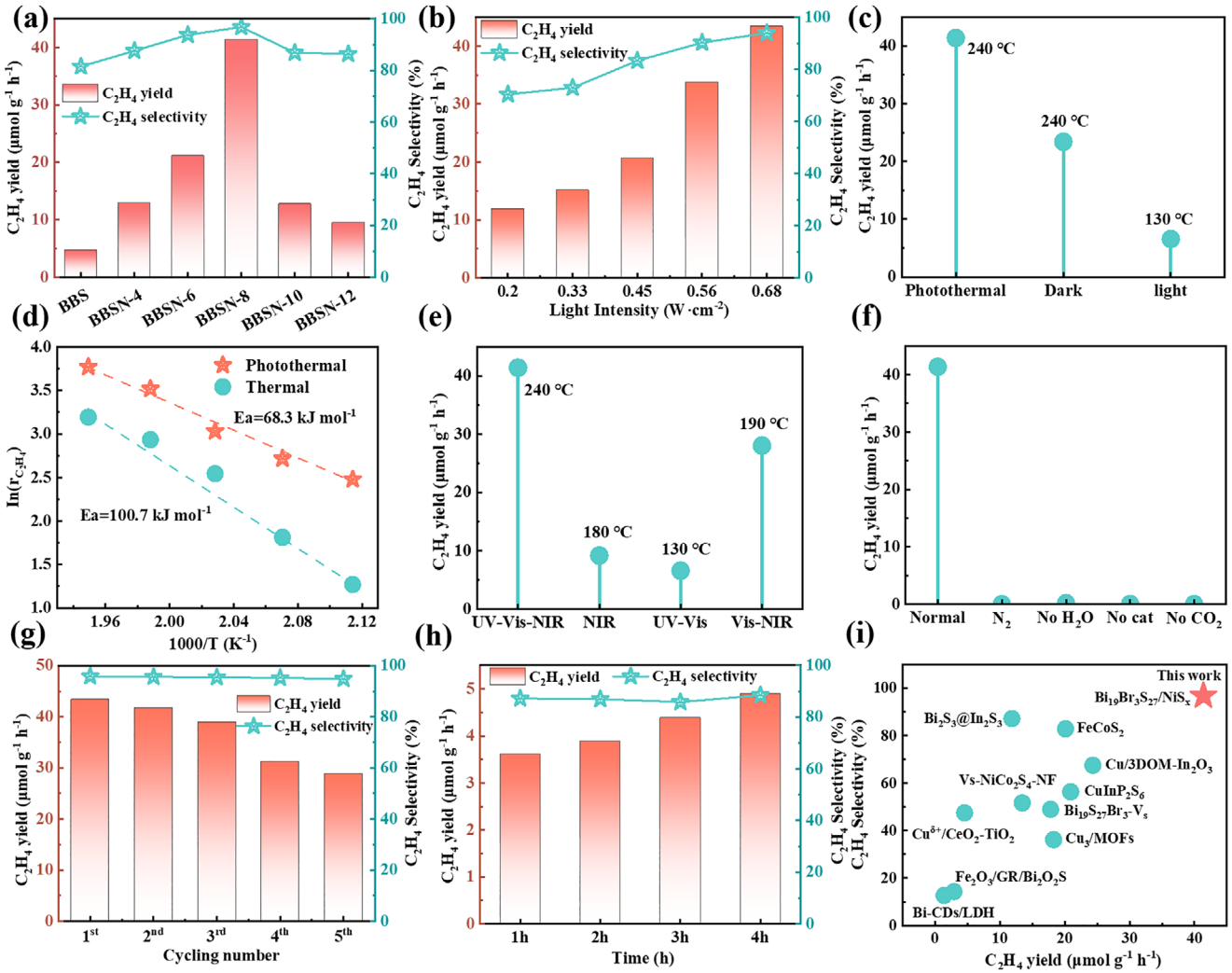

FIGURE 3 | (a) C_2H_4 yields and selectivity of CO_2 reduction on BBS and BBSN under full-spectrum light irradiation. C_2H_4 yields and selectivity of CO_2 reduction on BBSN-8 at different (b) irradiation intensities and (c) reaction system. (d) Apparent activation energy of BBSN-8 under photothermal conditions and in dark. C_2H_4 yields on BBSN-8 under different (e) light source irradiation and (f) reaction atmospheres. (g) Cycling tests of BBSN-8 for CO_2 reduction. (h) C_2H_4 yields and selectivity of BBSN-8 under atmospheric pressure conditions. (i) Comparison of the performance of BBSN-8 with reported catalysts in C_2H_4 production from CO_2.

observed under N_2 atmosphere or in the absence of CO_2 and catalyst. The $^{13}CO_2$ labeling experiment in Figure S11 further confirmed that the generated C_2H_4 originates exclusively from CO_2 reduction, rather than from any extraneous sources (The detected CO_2 signals arise from the filling of natural CO_2 into the reactor). The stability of the BBSN-8 catalyst is examined by cycling tests under full-spectrum illumination (Figure 3g). The C_2H_4 selectivity of the BBSN-8 is well maintained with slightly decreased yield in the CO_2 reduction reaction after five cycles. Besides, XRD and XPS analyses in Figure S12 before and after reaction confirm the good structural and chemical stability of BBSN-8. Moreover, the photothermal catalytic atmospheric CO_2 performance of the BBSN-8 is evaluated and shown in Figure 3h. Even under low CO_2 concentration conditions, BBSN-8 still has a good CO_2 reduction performance, in which the yield and selectivity of C_2H_4 could reach 4.9 μmol g^{-1} h^{-1} and 88.4%, respectively. In addition, it could be seen that BBSN-8 has a high selectivity for C_2H_4 than most reported catalysts (Figure 3i and Table S3). The results demonstrate that the BBSN-8 catalyst shows excellent photothermal catalytic CO_2 reduction with excellent C_2H_4 selectivity.

2.3 | Charge Carrier Separation Kinetics

The interfacial electron migration behavior in BBSN was further analyzed by combining XPS analysis with density functional theory (DFT) calculations. As displayed in Figure 4a, the Ni 2p XPS spectrum of BBSN-8 shows peaks at 853.7 and 871.4 eV corresponding to the Ni^{2+}, and peaks at 855.6 eV be assigned to the Ni^{3+} [30]. Under light irradiation, the binding energies of Ni in BBSN-8 shift toward lower values, whereas the of Bi shift toward higher energies (Figure 4b). This opposite shift indicates that photogenerated electrons migrate from BBS toward NiS_x, suggesting that NiS_x serve as co-catalyst and promotes interfacial electronic coupling [31]. To investigated the directional charge transfer, the work functions of BBS and NiS_x were calculated to be 5.036 and 5.257 eV, respectively (Figure 4c,d). Upon contact,

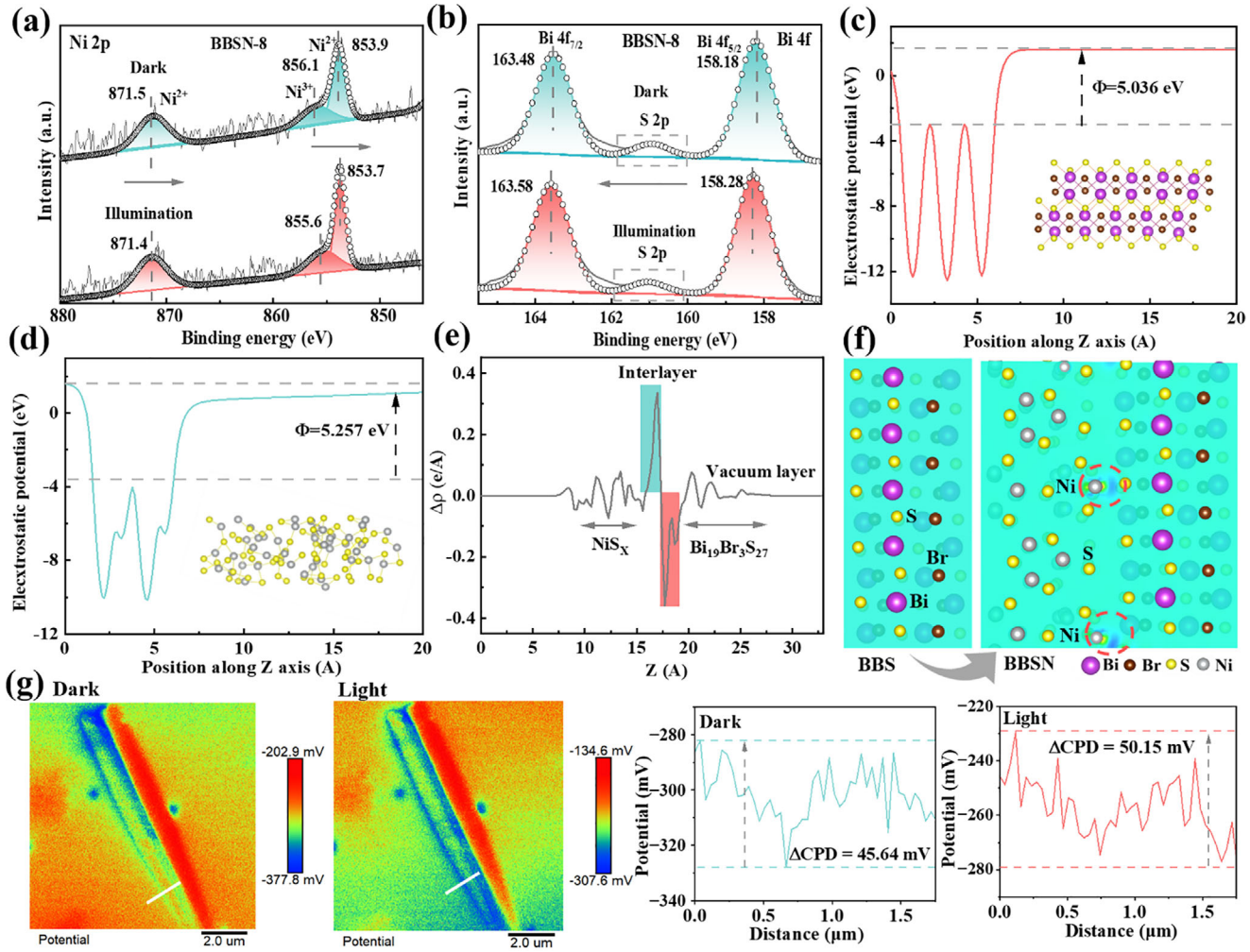

FIGURE 4 | (a) Ni 2p, (b) Bi 4f XPS spectra of BBSN-8 in dark and under light illumination. Electrostatic potentials of (c) BBS and (d) NiS_x. (e) The corresponding planar average differential charge in BBSN. (f) 2D charge density difference plot of BBSN. (g) Kelvin probe force microscopy (KPFM) surface potential maps and the corresponding line profiles of BBSN-8 in dark and under light irradiation.

the difference in Fermi levels (E_f) induces the migration of electrons from BBS to NiS_x, establishing an internal electric field (Figure 4e). Charge density difference calculations further confirm this process, where obvious electron accumulation occurs around the Ni sites in NiS_x region (Figure S13). Moreover, the 2D charge density difference plot in Figure 4f reveals a clear charge redistribution in BBSN. In BBS, the charge density is primarily confined around individual atomic sites, indicating limited electronic interaction between neighboring atoms. In contrast, the introduction of Ni induces distinct electron accumulation (green color) and depletion (blue color) regions around Ni sites. This spatial separation of charge suggests the formation of local dipoles and an internal electric field at the interface [32]. Furthermore, Bader charge analysis in Figure S14 was employed to quantitatively evaluate electron redistribution among Ni, S, and Bi atoms in BBSN. The results indicate that the Ni atom gains on average ~0.12 |e| from S, while each S atom accepts ~0.04 |e| from Bi within the Ni—S—Bi of BBSN, confirming that electrons are transferred from BBS to NiS_x. Additionally, DFT calculations further demonstrate that the distance between Bi and Ni decreases from 4.02 Å to 3.64 Å after interface formation (Figure S15), indicating that the formed Ni—S—Bi linkage effectively bridge Bi and Ni sites. The unique Ni—S—Bi bridge could induce strong orbital hybridization and establish spatially coupled dual-metal active sites capable of stabilizing reaction intermediates [1]. Based on these results, bandgap structure diagram and charge transfer mechanism for BBSN under light irradiation were proposed (Figure S16). Specifically, the built-in electric field accelerates separation and directional migration of photogenerated electrons from BBS to NiS_x, which favors the C—C coupling reaction.

The optical and electronic properties of BBSN were further examined. UV–Vis–NIR spectra in Figure S17 show that BBSN possesses stronger light absorption intensity than BBS across the entire spectral region. Meanwhile, the bandgap narrows from 1.55 eV for BBS to 1.48 eV for BBSN-8 (Figure S18), favoring NIR absorption and photothermal conversion. Furthermore, the results of Mott–Schottky tests show that the flat-band potential of BBSN-8 is −0.72 V vs. Ag/AgCl electrode, which could be estimated to be approximately −0.62 V due to *n*-type semiconductors (Figure S19) [33]. This is more negative than that of BBS (−0.49 V), which provides stronger reduction ability for CO_2 reduction to C_2H_4 ($E°(CO_2/C_2H_4)$ = −0.34 V vs. NHE, pH 7) (Figure S20).

Photoelectrochemical measurements further verify the enhanced carrier dynamics in BBSN. Compared with BBS, BBSN-8 displays a smaller arc diameter than that of BBS (Figure S21), indicating more efficient charge transfer and suppressed carrier recombination. The role of thermal excitation during the photothermal catalytic process was further clarified by temperature-dependent photoluminescence (TD-PL) spectra (Figure S22). A progressive decrease of PL intensity with rising temperature was observed, indicating that thermal energy promotes the separation of photogenerated carriers within BBSN [34]. In addition, the change in contact potential difference (ΔCPD) value of BBSN-8 increases from 45.64 mV in dark to 50.15 mV under illumination (Figure 4g), indicating an enhanced interfacial potential difference and more pronounced directional charge migration from BBS to NiS_x under light irradiation [35]. Additionally, surface charge properties were evaluated by zeta potential measurements (Figure S23). Introduction of NiS_x reversed the zeta potential of BBS from +5.62 mV to −0.22 mV, signifying an electron-rich surface state environment favorable for the adsorption and activation of CO_2 molecules, thereby contributing to improved catalytic activity.

2.4 | Theoretical Analysis of Orbital Hybridization

DFT theoretical calculations were carried out to elucidate the cooperative electronic interactions within the Ni—S—Bi structure of BBSN-8. The crystal orbital Hamilton population (COHP) analysis provides direct insight into the enhanced C_2H_4 production upon Ni incorporation. In BBS, the adsorption is dominated by an excessively strong Bi—C interaction (−3.43 eV), which may lead to over-stabilization of intermediates and hinder their subsequent coupling (Figure 5a) [36, 37]. After introducing Ni, the Bi—C interaction is significantly weakened (−2.00 eV), while additional Ni—C interactions (−1.10 eV) are established, indicating a redistribution of carbon binding sites (Figure 5b). This moderated and diversified carbon-metal interaction is critical for preventing site poisoning and enabling sufficient mobility of intermediates [38]. Meanwhile, the enhanced Bi—O (−1.99 eV), Ni—O (−0.73 eV), and S—O (−0.51 eV) interactions suggest a strengthened stabilization of oxygen-containing intermediates, which facilitates maintain adsorption balance during reaction (Figure 5c,d). More importantly, this cooperative adsorption enables synergistic stabilization of both the electrophilic carbon and nucleophilic oxygen termini, thereby inducing pronounced molecular bending and facilitating π^* orbital activation of CO_2. Meanwhile, this process facilitates carbon-containing intermediates coverage and activation, thereby promoting C—C coupling and leading to the significantly increased C_2H_4 production.

The density of states (DOS) further clarifies the electronic structure reconstruction of BBS induced by Ni incorporation. For BBS in Figure 5e, the valence band is mainly composed of Bi 6p and S 3p states, while the conduction band is predominantly contributed by Bi 6p states, indicating a relatively localized electronic structure with limited orbital overlap near the E_f. The C 2p states originating from adsorbed CO_2 are weakly distributed, suggesting localized electronic coupling and insufficient activation ability [39]. After Ni incorporation (Figure 5f), a pronounced Ni 3d state emerges near the E_f, spanning approximately from −2 to 0 eV, which significantly alters the interfacial electronic structure [40]. Notably, the Ni 3d orbitals exhibit strong hybridization with Bi 6p and S 3p states in this energy region, forming a continuous electronic distribution across the interface. More importantly, a clear overlap between Ni 3d, Bi 6p, and the C 2p states is observed near the E_f, implying strengthened orbital interaction between the catalyst surface and CO_2 [41, 42]. Compared with the results of DOS for BBS, the C 2p states in reaction of BBSN with CO_2 become more broadened and shift closer to the E_f, suggesting enhanced electronic coupling and improved ability for charge transfer from BBSN into CO_2 antibonding orbitals, which is consistent with the COHP results, where the adsorption configuration evolves from a single-site strong Bi—C interaction to a multi-site cooperative binding mode involving Bi—C, Bi—O, S—O, and Ni—C, which is beneficial for CO_2 activation and the enhanced C—C coupling performance.

As shown in Figure 5g, the S 3p orbitals act as an electronic bridge, simultaneously interacting with Bi 6p and Ni 3d states to form p-p and p-d hybridizations, respectively. Specifically, electron donation from S to the empty Bi 6p orbitals establishes a donor–acceptor p-p interaction, rendering the Bi sites electron-deficient. Meanwhile, the strong p-d hybridization between S 3p and Ni 3d orbitals proceeds via dual channels, involving π-type coupling with t_{2g} orbitals and σ-type interaction with e_g orbitals, thereby constructing a continuous electron transport network and enabling cross-interface charge delocalization [18, 43, 44]. Furthermore, as shown in Figure 5h, such electronic structure reconstruction markedly alters the adsorption and activation behavior of CO_2. In contrast to Bi sites, which interact with CO_2 primarily through weak p-π^* coupling leading to limited polarization, Ni sites provide both σ donation and π back-donation pathways. In particular, electron back-donation from Ni t_{2g} orbitals to the π^* antibonding orbitals of CO_2 effectively weakens the C═O bonds, thereby facilitating CO_2 activation.

2.5 | Investigation of C—C Coupling Mechanisms

To explore the greatly improved photothermal catalytic activity of CO_2 reduction with BBSN-8, comprehensive structural and electronic characterizations were conducted. The Brunauer–Emmett–Teller (BET) surface area of BBSN-8 was measured to be 65.026 $m^2\ g^{-1}$, which was larger than that of BBS (18.63 $m^2\ g^{-1}$), thereby providing more accessible sites for CO_2 adsorption (Figure S24 and Table S4). CO_2 temperature-programmed desorption (CO_2-TPD) tests in Figure 6a were directly used to reflect the adsorption ability of BBSN-8 and BBS for CO_2. Compared with BBS, BBSN-8 displays a pronounced desorption peak in the range of 200 to 400°C, indicating that BBSN-8 has stronger affinity for CO_2 compared to BBS [45]. DFT calculations were further performed to investigate the adsorption behavior of CO_2 on BBS and BBSN-8. The optimized adsorption configurations for BBS and BBSN reveal that the C in CO_2 is adsorbed on Bi and/or Ni, indicating that the C in CO_2 is more easily adsorbed on the surface of Bi or Ni. The adsorption energy of CO_2 on BBS is calculated to be −0.36 eV (Figure 6b), suggesting a relatively weak interaction with BBS. After the incorporation of NiS_x, the adsorption energy at the Bi sites of BBSN-8 decreases significantly to −1.452 eV. More importantly, when CO_2 is located at the interface between Bi and Ni sites, the adsorption energy further decreases to −2.185 eV, demonstrating that the Bi—Ni dual sites constitute the most favorable adsorption configuration with strong syn-

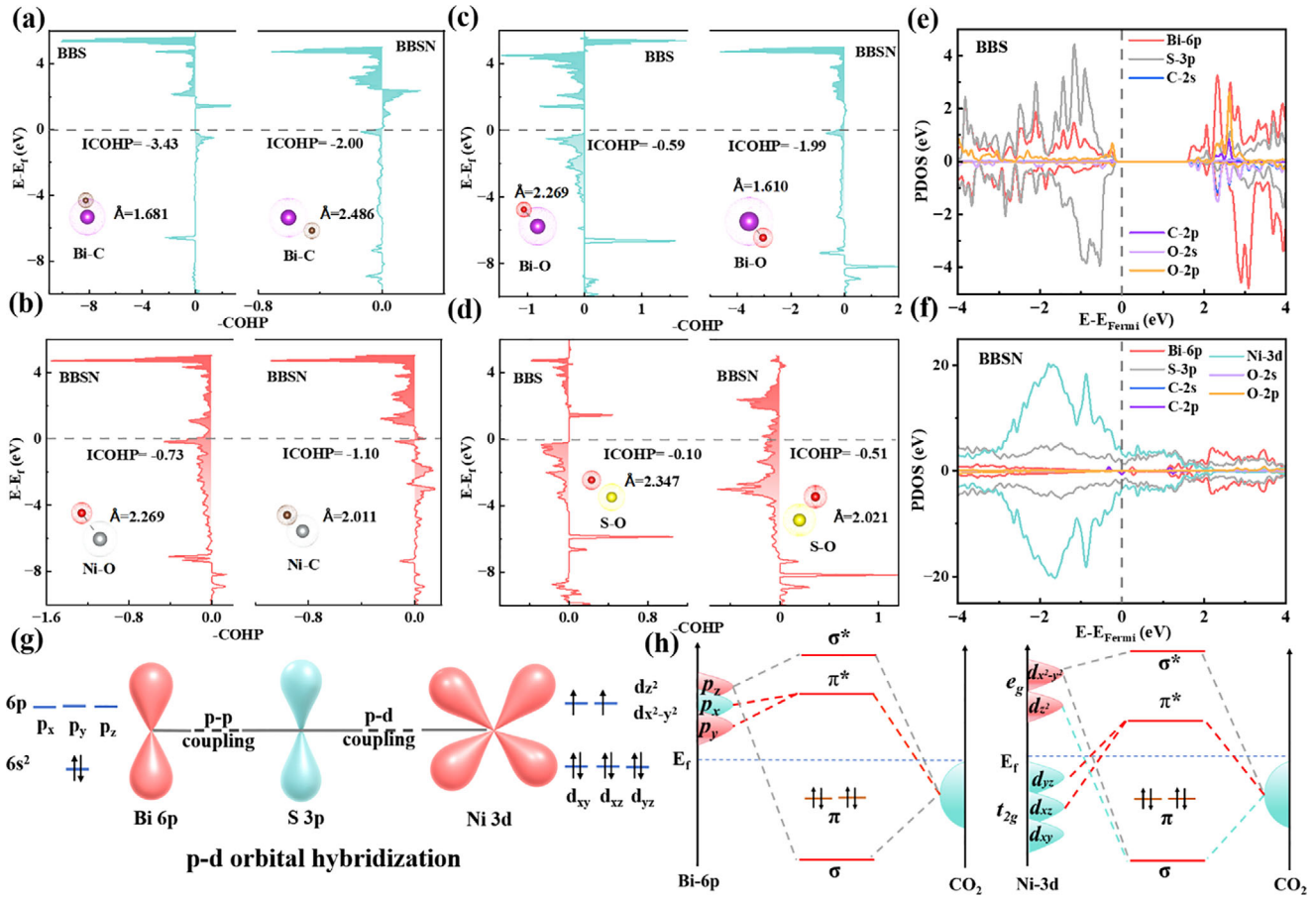

FIGURE 5 | COHP analysis of (a) Bi—C bond, (b) Ni—O and Ni—C, (c) Bi—O, (d) S—O of BBS and BBSN-8 react with CO_2, respectively. DOS analysis showing CO_2 interaction with (e) BBS and (f) BBSN, respectively. (g) Schematic depiction of p-d orbital hybridization for BBSN. (h) Schematic energy-level diagram illustrating the orbital interactions between Bi/Ni states and CO_2 molecular orbitals in BBSN.

ergistic interaction. The Bader charges show that the charge transferred from BBSN and BBS to CO_2 is 0.48 e^-, 0.17 e^-, respectively (Figure S25), indicating that the Ni 3d orbitals strongly hybridize with the C 2p of CO_2, enabling effective electron back-donation.

In situ diffuse reflectance infrared Fourier transform spectroscopy (in situ DRIFTS) tests were employed to investigate the reaction intermediates in the photothermal catalytic CO_2 reduction. As shown in Figure 6c, several new peaks emerged in the in situ DRIFTS spectra of BBS during the illumination period from 0 to 30 min, indicating the generation of several different reaction intermediates. The presence of peaks at 1576 cm^{-1} corresponded to the COOH* intermediates, which was a key intermediate for the conversion of CO_2 to C_1 and other fuels [46]. Moreover, the peak observed at 1358, 1436, and 1506 cm^{-1} are identified as originating from the HCOO*, *HCO_3, and m-CO_3^{2-} groups, respectively [33, 47]. Similarly, the characteristic peak at 1717 cm^{-1} was attributed to the presence of the CHO* groups [48]. In contrast, new characteristic peaks appeared in the in situ DRIFTS spectra of BBSN-8 under the same conditions (Figure 6d). The peak at 1541 cm^{-1} is associated with *OCCOH [1], which is recognized as a key intermediate for C—C coupling and C_2H_4 generation. Meanwhile, the peak at 1684 cm^{-1} was ascribed to C_2H_4* stretching vibration of C_2H_4, confirming the formation of C_2H_4 [49, 50]. Notably, no detectable OCCOH* signal is observed on BBS, suggesting that the OCCOH* group may be a prominent intermediate in the CO_2 reduction reaction pathway facilitated by the BBSN. Besides, obvious *CO accumulation (2110 cm^{-1}) is detected on BBS, whereas the *CO signal on BBSN-8 becomes much weaker (Figure 6e), which may be due to the rapid conversion of *CO intermediates after Ni incorporation [51, 52]. To clarify this difference, CO adsorption behavior was further examined by CO-TPD and DFT calculations. As shown in Figure S26, the CO adsorption energy (E_{ads}) in BBSN (−1.628 eV) is much higher than that in BBS (−0.341 eV), suggesting that p-d orbital hybridization significantly strengthens CO adsorption stability. Meanwhile, the results of CO-TPD in Figure 6f show that BBSN-8 has a larger peak area around 200–400°C compared to BBS, further confirming that BBSN-8 has stronger CO adsorption ability. Therefore, the absence of detectable *CO in the in situ DRIFTS spectra of BBSN-8 may be attributed to the rapid conversion of *CO intermediates on the surface.

To gain deeper insight into the reaction energetics, Gibbs free energy calculation was further carried out. As shown in Figure 6g, the conversion of adsorbed CO_2 to the *COOH intermediate involves a pronounced uphill free energy of approximately 2.47 eV for BBS, identifying this step as the potential-determining step. Moreover, the subsequent generation of *OCCOH intermediate by C—C coupling reaction between *CO and CHO*, requires an additional energy input of about 1.22 eV, indicating that

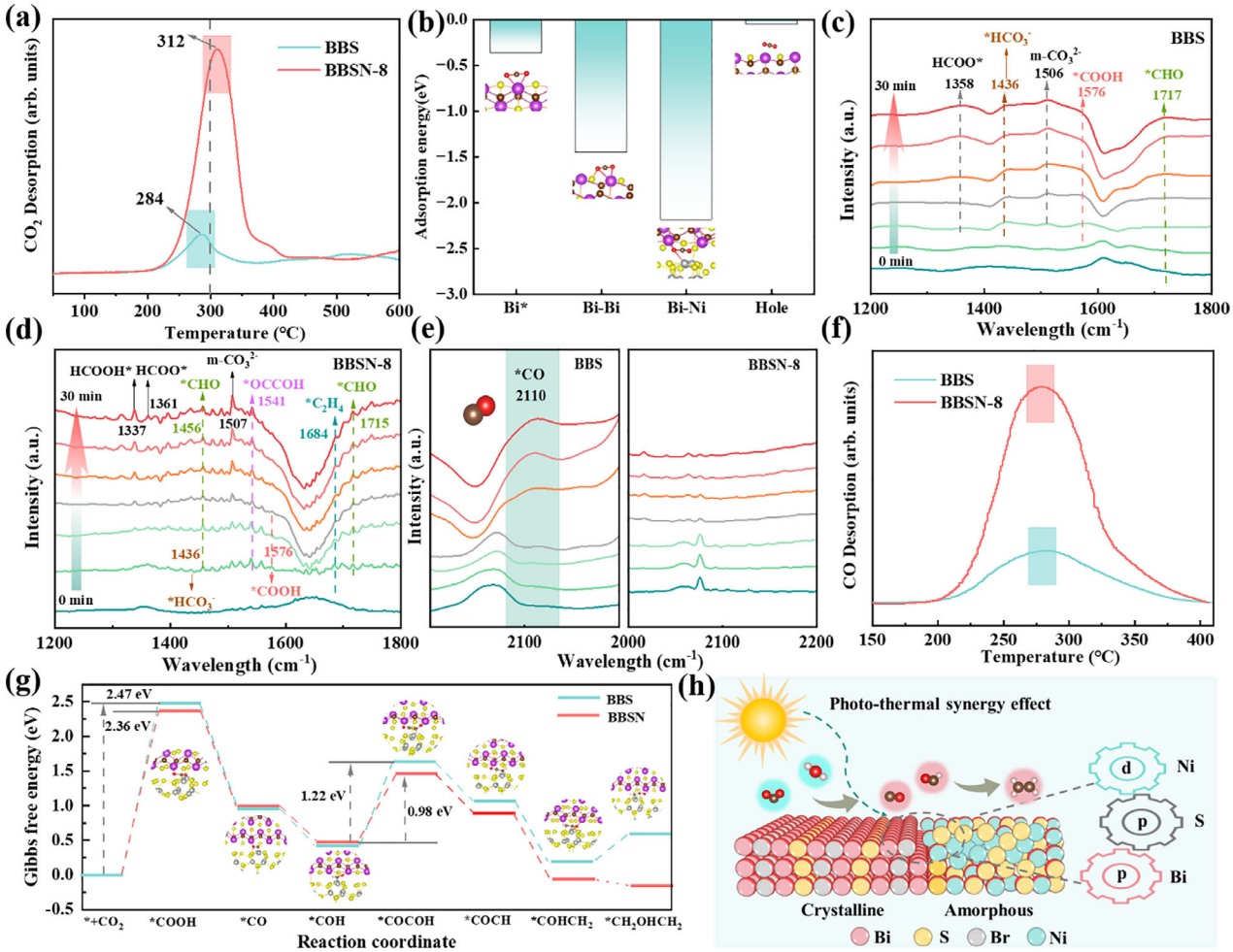

FIGURE 6 | (a) CO_2-TPD curve of BBS and BBSN-8. (b) Adsorption energy of CO_2 at different adsorption sites in BBS and BBSN. In situ DRIFTS for photothermal catalytic CO_2 reduction of (c) BBS and (d) BBSN-8 under full-spectrum irradiation. (e) Enlarged in situ DRIFTS of BBS and BBSN-8 under full-spectrum irradiation. (f) CO-TPD curve of BBS and BBSN-8. (g) Gibbs free energy diagrams of CO_2 reduction process over the BBS and BBSN. (h) The schematic diagram of photothermal catalytic CO_2 reduction into C_2H_4 for BBSN.

the formation of C_2 intermediates is more thermodynamically unfavorable on the surface of BBS [53]. In contrast, BBSN exhibits a slightly reduced free energy barrier of approximately 2.36 eV for the formation of the COOH* intermediate, suggesting a modest enhancement in CO_2 activation. More importantly, the free energy requirement for the formation of the *OCCOH intermediate is significantly decreased to around 0.98 eV, representing a substantial reduction compared to BBS, which greatly facilitates the C—C coupling process [54]. Furthermore, the subsequent intermediates along the C_2 pathway, such as *COCH and *$COHCH_2$ species, display more negative ΔG values on BBSN, indicating that the surface of BBSN is more conducive to C—C coupling reaction. As illustrated in Figure 6h, under photo-thermal synergy, newly formed p-d orbital coupling at the BBSN interface promotes charge redistribution and selective C_2H_4 formation via facilitated C—C coupling.

3 | Conclusion

In summary, an in situ constructed crystalline/amorphous $Bi_{19}Br_3S_{27}/NiS_x$ heterostructure was developed for highly selective photothermal CO_2 conversion toward C_2H_4. The optimized BBSN-8 catalyst achieved a C_2H_4 production rate of 41.38 μmol g^{-1} h^{-1} with a selectivity of 96.8%, representing an 8.8-fold enhancement over pristine $Bi_{19}Br_3S_{27}$. Mechanistic investigations reveal that the in situ generated NiS_x induces strong p-d orbital hybridization and transforms CO_2 activation from localized Bi—C single-site adsorption into a cooperative multi-site configuration involving Bi—C, Bi—O, S—O, and Ni—C interactions. Consequently, the C—C coupling barrier is significantly reduced, accompanied by the emergence of *OCCOH intermediates and suppressed *CO accumulation, thereby promoting selective C_2H_4 formation. This work highlights orbital-coupling-driven pathway regulation as an efficient strategy for selective multi-carbon photothermal catalytic CO_2 conversions.

Author Contributions

Guangmei Gan: software, data curation, formal analysis, validation, writing - original draft. **Zhixiong Yang**: formal analysis, data curation, writing – review and editing. **Mengying Wang**: data curation, validation. **Yang Shi**: writing – review and editing, formal analysis, validation. **Yuan Li**: writing – review and editing, validation. **Gaoke Zhang**: conceptualization, investigation, funding acquisition, writing – review

and editing, methodology, project administration, supervision, resources. **Jie Wu**: funding acquisition, writing – review and editing, supervision.

Acknowledgments

This work was supported by the National Natural Science Foundation of China (NSFC, No. 22361132537), Science and Technology Innovation Base Foundation of Hubei Province (2025CSA082) and Hubei Province Science and Technology Innovation Talent Plan (2023DJC135), Prime Minister's Office of Singapore under its NRF-CRP Programme (NRF-CRP29-2022-0004).

Conflicts of Interest

The authors declare no conflicts of interest.

Data Availability Statement

The data that supports the findings of this study are available in the Supporting Information of this article.

References

1. W. T. Song, C. Wang, Y. Liu, et al., "Unlocking Copper-Free Interfacial Asymmetric C−C Coupling for Ethylene Photosynthesis From CO_2 and H_2O," *Journal of the American Chemical Society* 146 (2024): 29028–29039, https://doi.org/10.1021/jacs.4c10023.

2. J. C. Wu, F. Huang, Q. Y. Hu, et al., "Regulated Photocatalytic CO_2-to-CH_3OH Pathway by Synergetic Dual Active Sites of Interlayer," *Journal of the American Chemical Society* 146 (2024): 26478–26484, https://doi.org/10.1021/jacs.4c09841.

3. Y. X. He, L. Yin, N. N. Yuan, and G. K. Zhang, "Adsorption and Activation, Active Site and Reaction Pathway of Photocatalytic CO_2 Reduction: A Review," *Chemical Engineering Journal* 481 (2024): 148754, https://doi.org/10.1016/j.cej.2024.148754.

4. H. B. He, Y. Q. Ren, Y.-H. Zhu, et al., "Continuous Flow Photothermal Catalytic CO_2 Reduction: Materials, Mechanisms, and System Design," *ACS Catalysis* 15 (2025): 10480–10520, https://doi.org/10.1021/acscatal.5c02269.

5. J. X. Xiong, J. P. Ji, Q. Lei, et al., "Synergetic Energy Coupled Thermal Catalytic Systems for CO_2 Reduction," *eScience* 5 (2025): 100306, https://doi.org/10.1016/j.esci.2024.100306.

6. S. B. Ning, H. H. Ou, Y. G. Li, et al., "Co^0 -$Co^{\delta+}$ Interface Double-Site-Mediated C−C Coupling for the Photothermal Conversion of CO_2 Into Light Olefins," *Angewandte Chemie International Edition* 62 (2023): e202302253, https://doi.org/10.1002/anie.202302253.

7. Z. K. Xie, W. J. Cheng, H. Y. Luo, Y. Lei, and W. D. Shi, "Artificial Photothermal Synthesis of Hydrocarbons From CO_2 and H_2O," *Advanced Energy Materials* 16 (2025): 2501840, https://doi.org/10.1002/aenm.202501840.

8. X. Liu, T. Liu, T. Ouyang, J. G. Deng, and Z.-Q. Liu, "Ce^{3+}/Ce^{4+} Ion Redox Shuttle Stabilized $Cu^{\delta+}$ for Efficient CO_2 Electroreduction to C_2H_4," *Angewandte Chemie International Edition* 64 (2025): e202419796, https://doi.org/10.1002/anie.202419796.

9. G. M. Gan, L. Yin, X. T. Wang, J. Y. Xing, Y. Li, and G. K. Zhang, "Interface-Engineered S-scheme 2D/1D Heterojunction of $Cs_{0.32}WO_3/WO_3{\cdot}2H_2O$ for Boosted CO_2 Photoreduction: Synergistic Charge Separation and Activation," *Chinese Journal of Catalysis* 79 (2025): 219–230, https://doi.org/10.1016/s1872-2067(25)64818-2.

10. F. Raziq, C. Y. Feng, M. Hu, et al., "Isolated Ni Atoms Enable near-Unity CH_4 Selectivity for Photothermal CO_2 Hydrogenation," *Journal of the American Chemical Society* 146 (2024): 21008–21016, https://doi.org/10.1021/jacs.4c05873.

11. S. A. Chernyak, M. Corda, M. Marinova, et al., "Decisive Influence of SAPO-34 Zeolite on Light Olefin Selectivity in Methanol-Meditated CO_2 Hydrogenation Over Metal Oxide-Zeolite Catalysts," *ACS Catalysis* 13 (2023): 14627–14638, https://doi.org/10.1021/acscatal.3c03759.

12. L. Liang, L. Yang, T. Heine, et al., "Asymmetric Copper-Sulphur Sites Promote C–C Coupling for Selective CO_2 Electroreduction to C_2 Products," *Advanced Energy Materials* 14 (2024): 2304224, https://doi.org/10.1002/aenm.202304224.

13. X. W. Lv, J. X. Gong, S. Y. Wang, et al., "Engineering Orbital Hybridization in Advanced Electrocatalysts for Energy Conversion: Fundamentals, Modulations, and Perspectives," *Advanced Energy Materials* 15 (2025): 2501129, https://doi.org/10.1002/aenm.202501129.

14. X. W. Shi, Z. Q. Su, C. Deng, et al., "Amorphization-Induced d-Orbital Rearrangement in Ultrathin CoO Nanosheets With Strong d-p Interactions for Efficient CO_2 Photoreduction," *Advanced Materials* 37 (2025): e2508492, https://doi.org/10.1002/adma.202508492.

15. J. C. Liu, X. Z. Deng, R. Wu, et al., "Tailoring p-p Orbital Hybridization via Oxygen Vacancy in Bismuth Oxybromide Heterojunctions for Efficient Photocatalytic CO_2 Reduction," *Advanced Functional Materials* 36 (2026): e18449, https://doi.org/10.1002/adfm.202518449.

16. Y. S. Yang, F. L. Wang, W. Y. Lyu, et al., "Establishing 3d-4d Orbital Hybridization for Efficient Photothermal Catalytic CO_2 Hydrogenation," *Angewandte Chemie International Edition* 64 (2025): e202509855, https://doi.org/10.1002/anie.202509855.

17. Y. X. Tuo, J. Y. Qu, H. L. Sun, et al., "Reactant-Dependent Volcano Trends in Pt-Catalyzed Cycloalkane Dehydrogenation: Orbital Hybridization-Guided Design of Active Sites," *Nature Communications* 17 (2025): 90, https://doi.org/10.1038/s41467-025-66782-w.

18. Y. Zhang, F. F. Chen, X. Y. Yang, et al., "Electronic Metal-Support Interaction Modulates Cu Electronic Structures for CO_2 Electroreduction to Desired Products," *Nature Communications* 16 (2025): 1956, https://doi.org/10.1038/s41467-025-57307-6.

19. G. S. Zhou, X. L. Liu, Y. R. Xu, S. Feng, Z. Y. Lu, and Z. Q. Liu, "Enhancing d/p-2π^* Orbitals Hybridization via Strain Engineering for Efficient CO_2 Photoreduction," *Angewandte Chemie International Edition* 63 (2024): e202411794, https://doi.org/10.1002/anie.202411794.

20. P. S. Li, J. H. Bi, J. Y. Liu, et al., "p−d Orbital Hybridization Induced by p-Block Metal-Doped Cu Promotes the Formation of C_{2+} Products in Ampere-Level CO_2 Electroreduction," *Journal of the American Chemical Society* 145 (2023): 4675–4682, https://doi.org/10.1021/jacs.2c12743.

21. H. Y. Long, X. D. Zhang, Z. Y. Zhang, J. J. Zhang, J. G. Yu, and H. G. Yu, "Fine-Tuning d-p Hybridization in Ni-B_x Cocatalyst for Enhanced Photocatalytic H_2 Production," *Nature Communications* 16 (2025): 946, https://doi.org/10.1038/s41467-025-56306-x.

22. K. Z. Lai, Y. X. Sun, L. P. Li, X. Q. Shi, L. Ge, and Z.-Q. Liu, "Cu Sites d Orbital Regulation Enables Highly Efficient Photocatalytic CO_2-to-Ethylene Conversion," *Advanced Functional Materials* 36 (2026): e24582, https://doi.org/10.1002/adfm.202524582.

23. J. X. Feng, X. S. Wang, and H. Pan, "In-situ Reconstruction of Catalyst in Electrocatalysis," *Advanced Materials* 36 (2024): 2411688, https://doi.org/10.1002/adma.202411688.

24. Z. H. Ma, S. Q. Zhan, Y. L. Zhang, et al., "An Electron Transfer Mediated Mechanism for Efficient Photoreforming of Waste Plastics Using a Ni_3S_4/ZnCdS Heterojunction," *Advanced Materials* 37 (2025): e2416581, https://doi.org/10.1002/adma.202416581.

25. S. L. Li, R. G. Ma, J. C. Hu, et al., "Coordination Environment Tuning of Nickel Sites by Oxyanions to Optimize Methanol Electro-Oxidation Activity," *Nature Communications* 13 (2022): 2916, https://doi.org/10.1038/s41467-022-30670-4.

26. R. R. Niu, Q. Y. Liu, B. J. Huang, et al., "Black Phosphorus/$Bi_{19}Br_3S_{27}$ van Der Waals Heterojunctions Ensure the Supply of Activated Hydrogen for Effective CO_2 Photoreduction," *Applied Catalysis B: Environmental* 317 (2022): 121727, https://doi.org/10.1016/j.apcatb.2022.121727.

27. W. L. Xu, R. Zhao, Q. Q. Li, et al., "Overall Water Splitting on the NiS/NiS_2 Heterostructures Featuring Self-Equilibrium Orbital Occu-

pancy," *Advanced Energy Materials* 13 (2023): 2300978, https://doi.org/10.1002/aenm.202300978.

28. J. H. Chen, Y. Q. Ren, Y. W. Fu, et al., "Integration of Co Single Atoms and Ni Clusters on Defect-Rich ZrO_2 for Strong Photothermal Coupling Boosts Photocatalytic CO_2 Reduction," *ACS Nano* 18 (2024): 13035–13048, https://doi.org/10.1021/acsnano.4c01637.

29. Q. Li, C. Q. Wang, H. L. Wang, J. Chen, J. Chen, and H. P. Jia, "Disclosing Support-Size-Dependent Effect on Ambient Light-Driven Photothermal CO_2 Hydrogenation Over Nickel/Titanium Dioxide," *Angewandte Chemie International Edition* 63 (2024): e202318166, https://doi.org/10.1002/anie.202318166.

30. H. G. Edao, C. Y. Chang, W. B. Dilebo, et al., "Nickel-Iron Layered Double Hydroxides/Nickel Sulfide Heterostructured Electrocatalysts on Surface-Modified Ti Foam for the Oxygen Evolution Reaction," *ACS Applied Materials & Interfaces* 16 (2024): 50602–50613, https://doi.org/10.1021/acsami.4c08215.

31. M. C. Liu, Y. B. Chen, J. Z. Su, J. W. Shi, X. X. Wang, and L. J. Guo, "Photocatalytic Hydrogen Production Using Twinned Nanocrystals and an Unanchored NiS_x Co-Catalyst," *Nature Energy* 1 (2016): 16151, https://doi.org/10.1038/nenergy.2016.151.

32. S. K. Xue, W. Q. Huang, W. Lin, et al., "Interfacial Engineering of Lattice Coherency at ZnO-ZnS Photocatalytic Heterojunctions," *Chem Catalysis* 2 (2022): 125–139, https://doi.org/10.1016/j.checat.2021.11.019.

33. J. Li, W. F. Pan, Q. Y. Liu, et al., "Interfacial Engineering of $Bi_{19}Br_3S_{27}$ Nanowires Promotes Metallic Photocatalytic CO_2 Reduction Activity Under Near-Infrared Light Irradiation," *Journal of the American Chemical Society* 143 (2021): 6551–6559, https://doi.org/10.1021/jacs.1c01109.

34. S. P. Mo, X. Y. Zhao, S. D. Li, et al., "Non-Interacting Ni and Fe Dual-Atom Pair Sites in N-Doped Carbon Catalysts for Efficient Concentrating Solar-Driven Photothermal CO_2 Reduction," *Angewandte Chemie International Edition* 62 (2023): e202313868, https://doi.org/10.1002/anie.202313868.

35. K. Yan, D. H. Wu, T. Wang, et al., "Highly Selective Ethylene Production From Solar-Driven CO_2 Reduction on the Bi_2S_3@In_2S_3 Catalyst With In–S_V–Bi Active Sites," *ACS Catalysis* 13 (2023): 2302–2312, https://doi.org/10.1021/acscatal.2c05741.

36. A. Y. Meng, X. Y. Wu, Z. W. Lu, et al., "Accelerated Interfacial Charge Transfer via Ni 3d-S 3p Orbital Hybridization in a CdS/NiPc S-Scheme Heterojunction for Highly-Selective H_2O_2 Photosynthesis," *Angewandte Chemie International Edition* 65 (2026): e25871, https://doi.org/10.1002/anie.202525871.

37. Y. Q. Zhang, M. Liu, L. T. Zhang, et al., "Strategic Defect Engineering Enabled Efficient Oxygen Evolution Reaction in Reconstructed Metal-Organic Frameworks," *Advanced Functional Materials* 35 (2025): 2412406, https://doi.org/10.1002/adfm.202412406.

38. J. T. Li, L. M. Liu, D. H. Guan, et al., "d-p Orbital Hybridization Tailoring for Boosted Redox Kinetics in Li-CO_2 Batteries," *Advanced Functional Materials* 36 (2026): e14223, https://doi.org/10.1002/adfm.202514223.

39. F. Y. Chen, G. Q. Cao, Q. Liu, Y. N. Duan, W. Z. Li, and Z. R. Shen, "Bi–O Bridges Trigger Lattice Strain-Electronic Synergy at Inherent In Sites in $ZnIn_2S_4$ for Boosting Solar-to-H_2O_2 Conversion," *Angewandte Chemie International Edition* 64 (2025): e202518232, https://doi.org/10.1002/anie.202518232.

40. X. Zhang, Q. X. Zhou, C. Li, et al., "Thermodynamic and Kinetic Modulation of Artificial H_2O_2 Photosynthesis via Spatial Control of Redox Catalytic Sites," *Journal of the American Chemical Society* 148 (2026): 11068–11080, https://doi.org/10.1021/jacs.5c22625.

41. H. Y. Long, R. N. Li, C. B. Bie, et al., "Self-Disproportionation-Induced H-Adsorption/Desorption Zones in Amorphous Nickel Boride Cocatalyst for Efficient Photocatalytic Hydrogen Evolution," *Journal of the American Chemical Society* 148 (2026): 17146–17156, https://doi.org/10.1021/jacs.6c01844.

42. C. X. Yin, Z. C. Sun, K. L. Tang, et al., "Asymmetric Charge-polarization Tailoring Active Hydrogen Transfer for Selective Photoreduction CO_2 to CH_4," *Nature Communications* 17 (2026): 5142, https://doi.org/10.1038/s41467-026-71695-3.

43. S. J. Shen, J. Y. Li, X. Li, J. L. Wang, C. L. Zhang, and F. Dong, "Kinetics-Controlled Radical Coupling on Dual Redox-Active Sites for Selective Formamide Production," *Nature Communications* 17 (2026): 5472, https://doi.org/10.1038/s41467-026-72215-z.

44. J. W. Li, T. C. Xiang, X. Liu, M. N. Ghazzal, and Z.-Q. Liu, "Structure-Function Relationship of p-Block Bismuth for Selective Photocatalytic CO_2 Reduction," *Angewandte Chemie International Edition* 63 (2024): e202407287, https://doi.org/10.1002/anie.202407287.

45. L. F. Liu, D. Z. Chen, H. X. Yan, Y. H. Zhang, X. K. Wang, and M. Wang, "A Donor-Acceptor Porous Organic Polymer Anchoring a High Density of Cobalt Single Sites Realizes Full-Spectrum Photothermal CO_2 Hydrogenation," *Chem* 12 (2026): 102905, https://doi.org/10.1016/j.chempr.2025.102905.

46. R. N. Wang, M. J. Zhang, J. J. Liu, et al., "Defect-Phase Engineered NiTi-TiO_2 Enabling near-Unity Selective Photocatalytic CO_2-to-Methanol Conversion," *Nature Communications* 16 (2025): 7844, https://doi.org/10.1038/s41467-025-63179-7.

47. J. Wu, X. D. Li, W. Shi, et al., "Efficient Visible-Light-Driven CO_2 Reduction Mediated by Defect-Engineered BiOBr Atomic Layers," *Angewandte Chemie International Edition* 57 (2018): 8719–8723, https://doi.org/10.1002/anie.201803514.

48. N. X. Li, R. M. Jiang, Y. Li, et al., "Plasma-Assisted Photocatalysis of CH_4 and CO_2 Into Ethylene," *ACS Sustainable Chemistry & Engineering* 7 (2019): 11455–11463, https://doi.org/10.1021/acssuschemeng.9b01284.

49. Y. Xu, P. Wang, M. Zhang, et al., "Constructing Asymmetric Dual Active Sites Through Symbiotic Effect for Achieving Efficient and Selective Photoreduction of CO_2 to C_2H_4," *Energy & Environmental Science* 17 (2024): 5060–5069, https://doi.org/10.1039/d4ee01376j.

50. Y. Y. Yu, Y. He, P. Yan, S. Y. Wang, and F. Dong, "Boosted C–C Coupling With Cu-Ag Alloy Sub-Nanoclusters for CO_2-to-C_2H_4 Photosynthesis," *Proceedings of the National Academy of Sciences* 120 (2023): e2307320120, https://doi.org/10.1073/pnas.2307320120.

51. C. Sun, J. L. Yin, and H. H. Fei, "Highly Stable π-Extended Viologen Functionalized Hybrid Lead Halides for Near Infrared-Driven CO_2-to-C_2H_4 Photoconversion," *Angewandte Chemie International Edition* 64 (2025): e202514206, https://doi.org/10.1002/anie.202514206.

52. Y. Y. Zhang, Y. X. Chen, X. W. Wang, et al., "Low-Coordinated Copper Facilitates the *CH_2CO Affinity at Enhanced Rectifying Interface of Cu/Cu_2O for Efficient CO_2-to-Multicarbon Alcohols Conversion," *Nature Communications* 15 (2024): 5172, https://doi.org/10.1038/s41467-024-49247-4.

53. Z. K. Xie, S. J. Xu, L. H. Li, et al., "Well-Defined Diatomic Catalysis for Photosynthesis of C_2H_4 From CO_2," *Nature Communications* 15 (2024): 2422, https://doi.org/10.1038/s41467-024-46745-3.

54. P. J. Du, J. Y. Ding, C. Y. Liu, et al., "Interface-Engineering-Induced C–C Coupling for C_2H_4 Photosynthesis From Atmospheric–Concentration CO_2 Reduction," *Angewandte Chemie International Edition* 64 (2025): e202421353, https://doi.org/10.1002/anie.202421353.

Supporting Information

Additional supporting information can be found online in the Supporting Information section.

Supporting File: anie74821-sup-0001-SuppMat.docx.